Probing the Néel Order in Altermagnetic RuO_2 Films via X-Ray Magnetic Linear Dichroism

Yi-Chi Zhang(张一弛)[1,2], Hua Bai(白桦)[1], Dong-Hui Zhang(张东辉)[1], Chong Chen(陈崇)[1], Lei Han(韩磊)[1], Shi-Xuan Liang(梁诗萱)[1], Rui-Yue Chu(褚瑞月)[1], Jian-Kun Dai(戴健坤)[1], Maciek Sawicki[3], Feng Pan(潘峰)[1], and Cheng Song(宋成)[1*]

[1]*Key Laboratory of Advanced Materials (MOE), School of Materials Science and Engineering, Tsinghua University, Beijing 100084, China*
[2]*Key Laboratory of Materials Modification by Laser, Ion and Electron Beams (MOE), Dalian University of Technology, Dalian 116024, China*
[3]*Institute of Physics, Polish Academy of Sciences, Aleja Lotnikow 32/46, PL-02668 Warsaw, Poland*

(Received 14 December 2024; accepted manuscript online 7 January 2025)

The emerging altermagnetic RuO_2 with both compensated magnetic moments and broken time-reversal symmetry possesses nontrivial magneto-electronic responses and nonrelativistic spin currents that are closely related to the magnetic easy axis. Ru M_3-edge X-ray magnetic linear dichroism (XMLD) measurements were performed to probe the Néel order in RuO_2. For epitaxial RuO_2 films, characteristic XMLD signals were observed for either RuO_2(100) or RuO_2(110) at normal incidence or RuO_2(001) at oblique incidence. The signals disappeared when the test temperature exceeded the Néel temperature. For non-epitaxial RuO_2 films, the flat lines in the XMLD patterns of RuO_2(100) and RuO_2(110) demonstrate that there is no in-plane uniaxial alignment of the Néel order in these samples because of the counterbalanced Néel order of the twin crystals, as evidenced by X-ray diffraction phi-scan measurements. Our experimental results unambiguously demonstrate antiferromagnetism in RuO_2 films and reveal the spatial relation of the Néel order parallel to the RuO_2 [001] crystalline axis. These findings deepen the understanding of RuO_2 and other attractive altermagnetic materials used in the field of spintronics.

DOI: 10.1088/0256-307X/42/2/027301 CSTR: 32039.14.0256-307X.42.2.027301

Recently, altermagnetism has attracted considerable research attention because it simultaneously possesses broken time-reversal symmetry and compensated magnetic moments, which are typical features of ferromagnetism and conventional antiferromagnetism, respectively.[1–9] Among many altermagnetic materials, RuO_2, which has considerable spin-splitting energy, has a relatively high Néel temperature ($T_N > 300$ K) and metallic conduction, which are beneficial for spintronic applications.[10–14] Based on the alternating magnetic spin-splitting effect (ASSE), RuO_2 also possesses nontrivial magneto-electronic responses, including the anomalous Hall effect (AHE), and it is able to generate nonrelativistic spin currents, which are closely associated with the magnetic structure and magnetic easy axis.[14,15]

Contrary to conventional antiferromagnets with combined real-space inversion and time-reversal (PT) symmetry, the AHE has been theoretically predicted and experimentally observed to exist in altermagnetic RuO_2 with broken PT symmetry.[14,16–19] According to vector magnetometry and magneto-transport measurements, the AHE is ascribed to the reversal of a Berry curvature hotspot induced by the rotation of the Néel order.[18,19] A change in the magnetic easy axis results in a variation in the magnetic space group (or magnetic point group) and hence brings about new magneto-electronic responses.[20] The finite Hall vector cannot be obtained under symmetry operations unless the Néel order is altered from the [001] to either the [100] or [110] crystal axes in RuO_2.[14,18,21] In contrast, owing to ASSE, altermagnetic RuO_2 whose spin band splitting in momentum space is comparable to that of ferromagnets, can generate time-reversal-odd spin currents and spin splitting torque.[15,22–24] This nonrelativistic mechanism provides an alternative to efficiently manipulate magnetization in addition to common approaches, such as spin-transfer torque and spin-orbit torque.[25,26] Furthermore, this mechanism is free from the limitations of the orthogonal relation between the charge current, spin current, and spin polarization obeyed by the spin Hall effect resulting from geometric symmetry, and it can also break the inverse relation between the spin Hall angle and spin diffusion length that is followed by traditional relativistic spin sources.[27,28] In the case of the ASSE, the spin polarization was ascertained to be parallel to the direction of the Néel order.[22–24] Therefore, diverse magneto-electronic transport properties and nonrelativistic phenomena of spin currents in RuO_2 rely closely on the spatial relation of the antiferromagnetic Néel order with respect to the crystal orientation in RuO_2 films.

Previous works have studied and demonstrated antiferromagnetism in RuO_2 bulk and films via methods including polarized neutron diffraction,[11] resonant X-ray

*Corresponding author. Email: songcheng@mail.tsinghua.edu.cn
© 2025 Chinese Physical Society and IOP Publishing Ltd. All rights, including for text and data mining, AI training, and similar technologies, are reserved.

scattering,[12] magnetic circular dichroism,[29] and spin-ARPES.[30] However, a recent study adopted the muon spin-rotation technique to measure bulk RuO_2 and reported no antiferromagnetic order in RuO_2.[31] Furthermore, this controversial issue can be attributed to different Ru/O stoichiometric ratios in various RuO_2 samples.[32] Hence, it has become timely and important to elucidate the antiferromagnetic properties of RuO_2 with sufficient experimental evidence. To this end, X-ray magnetic linear dichroism (XMLD) combined with soft X-ray absorption spectroscopy (XAS) is an efficient technique for characterizing the antiferromagnetic Néel order.[33] In addition to being utilized to detect the compensated magnetic order in antiferromagnetic films,[34–36] XMLD can be applied to explore interfacial phenomena in heterostructures involving antiferromagnetic components[37–40] and demonstrate current-induced Néel order switching.[41,42] Apart from scanning the absorption edge of $3d$ transition metals,[43–46] XAS has also been applied to test Ru when investigating $SrRuO_3$, thus proving the feasibility of this technique for characterizing $4d$ transition metals.[47] In this study, we investigated RuO_2 films using XMLD together with X-ray diffraction and magnetization measurements. We observed the existence of an antiferromagnetic order and elucidated its spatial relationship with the crystalline orientation of altermagnetic RuO_2 films. The findings of this study deepen our understanding of antiferromagnetism in altermagnetic RuO_2, which is vital for elucidating the properties of altermagnets, such as spin splitting and unconventional spin current generation.

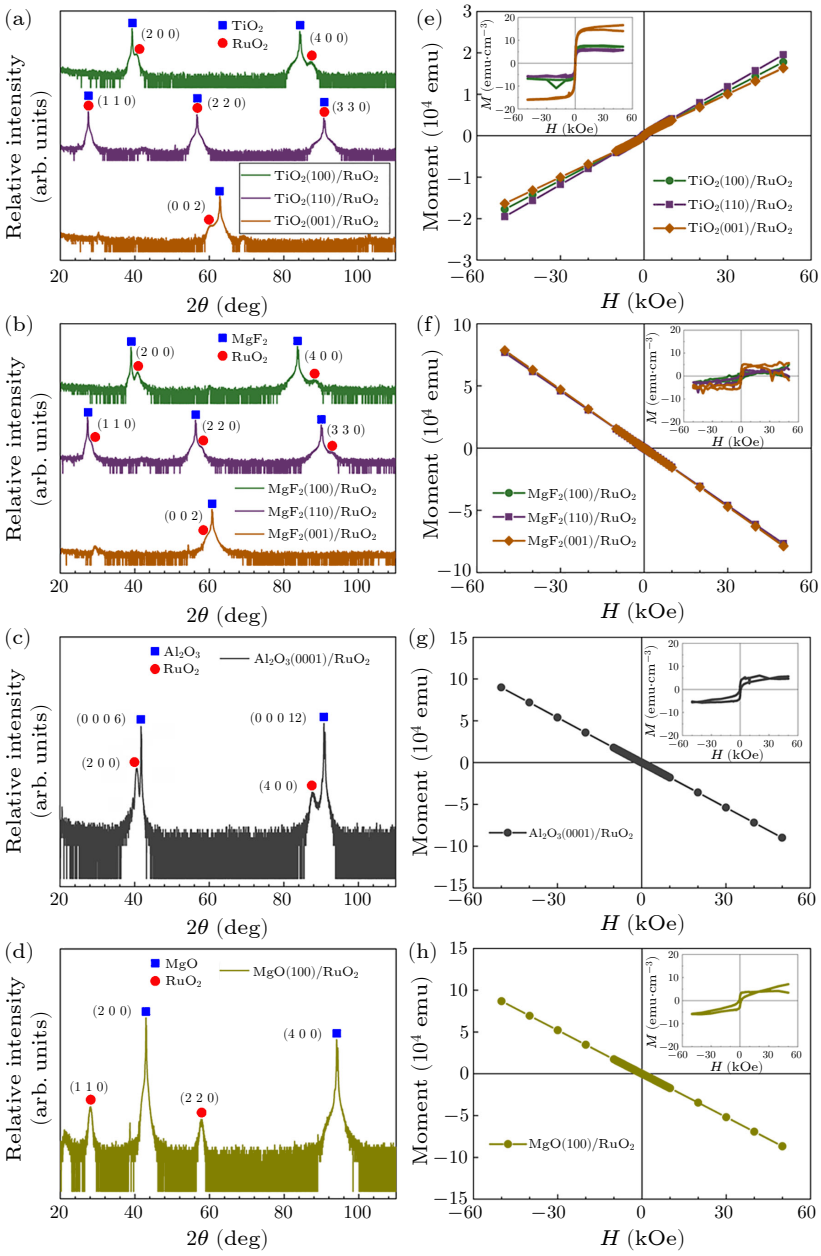

Fig. 1. XRD 2θ-ω diffraction patterns and M-H plots of RuO_2 films deposited on (a), (e) (100)-, (110)-, and (001)-oriented TiO_2 substrates; (b), (f) (100)-, (110)-, and (001)-oriented MgF_2 substrates; (c), (g) Al_2O_3(0001) substrate; and (d), (h) MgO(100) substrate, respectively. After the subtraction of a linear in H components representing background signals from substrates, the magnetization (M) curves of RuO_2 films are plotted in the insets of panels (e) through (h). All measurements are taken at 300 K.

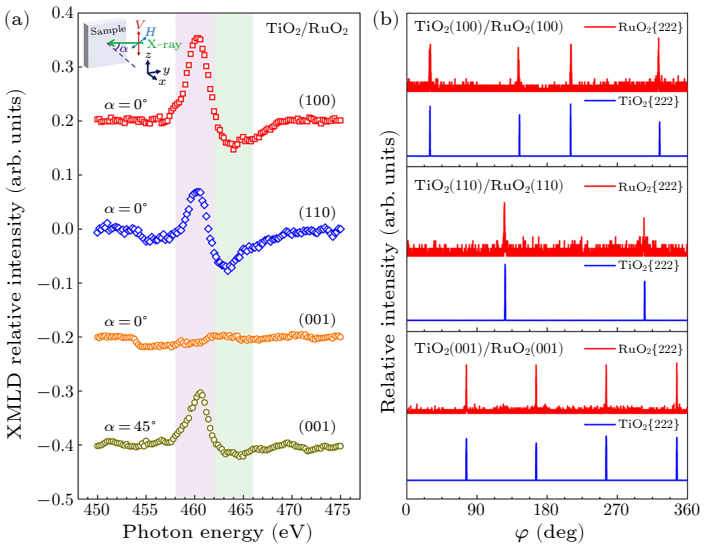

Fig. 2. XMLD and XRD patterns of epitaxial RuO_2 films on TiO_2 substrates. (a) XMLD patterns of RuO_2 films with (100), (110), and (001) crystalline orientations. (b) Phi-scan results of RuO_2 films with (100), (110), and (001) crystalline orientations. The inset of panel (a) illustrates the set-up of the XMLD measurements with an angle of α between the incident light and normal of the film plane.

To study the dependence of the Néel order on crystalline orientation, we sputtered RuO_2 films onto TiO_2, MgF_2, Al_2O_3, and MgO substrates (see Experimental Methods for more details). First, the phase composition and crystalline orientation are revealed by XRD patterns (2θ-ω scan), and the results are presented in Fig. 1 from panel (a) to (d). As shown in Figs. 1(a) and 1(b), each panel displays the results for RuO_2 films on single-crystal TiO_2 and MgF_2 substrates, respectively. Moreover, the diffraction peaks at $2\theta = 40°$, $28°$, and $60°$ (marked by red bullets) are observable in both panels, corresponding with the (100), (110), and (001) lattice planes of RuO_2. Hence, after the deposition of the RuO_2 films on the TiO_2 and MgF_2 substrates, the films share the same crystalline orientation as the substrates. RuO_2, TiO_2, and MgF_2 have rutile crystal structures, and some diffraction peaks of the films and substrates in Figs. 1(a) and 1(b) can hardly be distinguished from each other owing to their similar lattice parameters, which are prerequisites for the epitaxial growth mode of RuO_2 films on TiO_2 and MgF_2 substrates. In contrast, when they are sputtered on hexagonal $Al_2O_3(0001)$ and cubic MgO(100) substrates, the RuO_2 films are (100)- and (110)-oriented, as indicated by the characteristic peaks of $2\theta = 40°$ and $28°$ in Figs. 1(c) and 1(d), respectively. In such cases, the difference in the crystal structure and apparent lattice mismatch would result in a non-epitaxial growth mode of RuO_2 films on Al_2O_3 and MgO substrates. Next, the magnetization of RuO_2 film samples is measured using a superconducting quantum interference device (SQUID) at 300 K, and the dependence of the magnetic moment on the applied magnetic field is displayed in Fig. 1 from panels (e) through (h), with applied magnetic fields from −50 to 50 kOe. Upon applying the standard routine of subtracting the linear-in-H magnetic contribution to represent that of the substrates, step-like M–H curves emerge, as indicated by the insets in panels (e) through (h) of Fig. 1. These curves indicate a relatively large absolute contribution from unspecified magnetic contaminants present on or within the commercial substrates,[48,49] than that of the investigated signal from RuO_2, as the expected magnetic responses in altermagnets are very weak, as shown recently for bulk hexagonal MnTe.[50] Notably, TiO_2 is paramagnetic, whereas MgF_2, Al_2O_3, and MgO are diamagnetic. Therefore, contrary to the up-to-down tendency of the results presented in Figs. 1(f)–1(h), the M-H lines increase as the magnetic field increases, as shown in Fig. 1(e).

Then, we focused on the epitaxial RuO_2 films in terms of the distribution of the Néel order and in-plane crystal symmetry, which were characterized using Ru M_3-edge XMLD and XRD phi-scan methods, respectively. The inset of Fig. 2(a) shows the XMLD measurement setup, where the film sample was placed parallel to z-axis and the incident X-ray was perpendicular to the z-axis. Also, the purple dashed line indicates the normal of the film plane, which has an angle of α with respect to the incident X-ray. We measured XAS with linear horizontal and vertical polarizations, and the XMLD was the difference between the normalized XAS curves with two linear polarization modes. Figure 2(a) shows the XMLD results for the TiO_2-based film samples, and Fig. 2(b) shows the XRD phi-scan patterns. The Ru element M_3-edge is 462 eV, and within the nearby testing range, both $TiO_2/RuO_2(100)$ and $TiO_2/RuO_2(110)$ had zero-positive-negative-zero XMLD signals, whereas there were no characteristic peaks for the XMLD result of $TiO_2/RuO_2(001)$ in Fig. 2(a). The upper three curves in Fig. 2(a) are measured with $\alpha = 0°$ (with the incident light being perpendicular to the film plane), and after rotating the $TiO_2/RuO_2(001)$ sample around the z-axis so that the angle of incident α is changed from $0°$ to $45°$, we can again observe a zero-positive-negative-zero feature in the XMLD signals of $TiO_2/RuO_2(001)$ shown by the bottom (dark yellow) dots of Fig. 2(a), which is similar to those of $TiO_2/RuO_2(100)$ and $TiO_2/RuO_2(110)$. We scanned

the non-oriented plane of (222) for both the films and substrates of the three TiO_2/RuO_2 samples, as shown by the three pairs of XRD phi scan curves in Fig. 2(b). Considering the equal number and location of the diffraction peaks, the RuO_2 films had the same in-plane crystalline symmetry as did the TiO_2 substrates, thus indicating straightforward the epitaxial relationship of the RuO_2 films.

We also performed XMLD and XRD phi-scan measurements of MgF_2/RuO_2 with different crystal orientations, and the results are shown in Figs. 3(a) and 3(b), respectively. The (red) squares and (blue) diamonds in Fig. 3(a) demonstrate that the (100)- and (110)-oriented MgF_2/RuO_2 film samples also possess zero-positive-negative-zero XMLD signals at the Ru M_3-edge. However, no obvious peaks or valleys can be observed in (001)-oriented RuO_2 with $\alpha = 0°$, as displayed by the (orange) circles in Fig. 3(a). In terms of the incident X-ray, the rotation of the $MgF_2/RuO_2(001)$ sample around the z-axis with $\alpha = 45°$ leads to the nonzero in-plane component of the [001] crystal axis. Moreover, the characteristic XMLD pattern can be observed in the bottom (dark yellow) circles of Fig. 3(a). The XMLD results of the RuO_2 films on MgF_2 were consistent with those of their counterparts on the TiO_2 substrates. The epitaxial growth mode of MgF_2/RuO_2 was also supported by the congeneric phi-scan patterns shown in Fig. 3(b). Hence, for the epitaxial RuO_2 films, we observed the characteristic XMLD signals of either $RuO_2(100)$ and $RuO_2(110)$ at normal incidence or $RuO_2(001)$ at oblique incidence. Whether the crystalline axis is perpendicular to or lies in the film plane leads to the absence or existence of an in-plane distribution of the Néel order. Consequently, the Néel order in the RuO_2 films lies along the direction parallel to the [001] crystal axis of RuO_2.

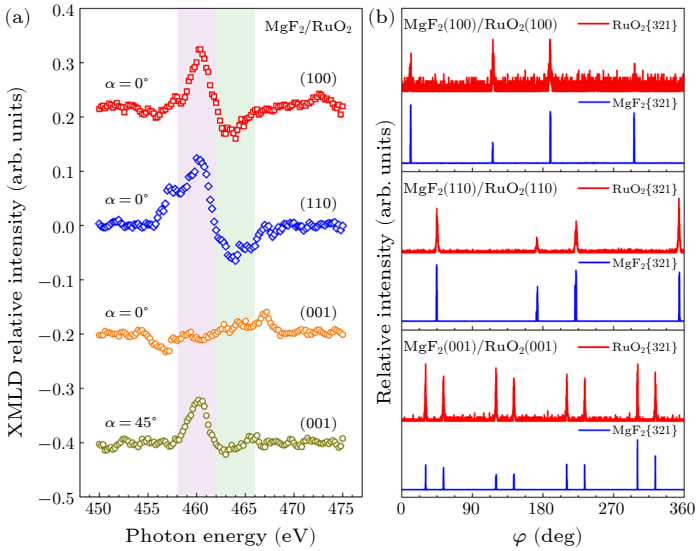

Fig. 3. XMLD and XRD patterns of epitaxial RuO_2 films on MgF_2 substrates. (a) XMLD patterns of RuO_2 films with (100), (110), and (001) crystalline orientations. (b) Phi-scan results of RuO_2 films with (100), (110), and (001) crystalline orientations.

Significantly, we also conducted temperature-dependent XMLD measurements below and above the Néel temperature and observed the disappearance of the characteristic XMLD patterns under the latter condition, which indicates that the detected characteristic XMLD signals originated from the antiferromagnetism of RuO_2 (see Note 1 of the Supplemental Material for details). Our experimental results obtained by XMLD are in good agreement with those of previous studies on the antiferromagnetism of RuO_2 via polarized neutron diffraction and resonant X-ray scattering,[11,12] and our results also support the transport measurements of RuO_2 films.[18,19,21]

Figures 4(a) and 4(b) show the corresponding XMLD results for non-epitaxial RuO_2 films grown on $Al_2O_3(0001)$ and MgO(100) substrates, respectively. The corresponding XRD phi-scan patterns are plotted in Figs. 4(c) and 4(d), respectively. According to the aforementioned XMLD results for epitaxial RuO_2 films on TiO_2 and MgF_2 substrates, the Néel order should lie in the plane for both the $Al_2O_3/RuO_2(100)$ and $MgO/RuO_2(110)$ samples. However, neither sample exhibited characteristic XMLD features, as evidenced by the flat curves within the relevant testing range in Figs. 4(a) and 4(b), which are opposite to those of their epitaxial counterparts. In addition, we scanned the $RuO_2(110)$ and $Al_2O_3(10\bar{1}4)$ crystalline planes for the film and substrate of the Al_2O_3/RuO_2 sample; the top and bottom patterns in Fig. 4(c) show six-fold and three-fold rotational symmetry, respectively. Considering the relevant lattice structure and parameters, there are three types of matching modes for Al_2O_3/RuO_2 with a rotation angle of 120°, as shown in the inset of Fig. 4(a). Similarly, we chose (111) as the non-oriented crystalline plane to conduct an XRD phi-scan of the MgO/RuO_2 sample. The evenly spaced diffraction peaks with an interval of 90° in both the top and bottom plots of Fig. 4(d) demonstrate four-fold rotation symmetry. Hence, two types of twin crystals exist in MgO/RuO_2, and their in-plane orientations are orthogonal to each other, as shown in the inset of Fig. 4(b). The XRD phi-scan results unambiguously reveal

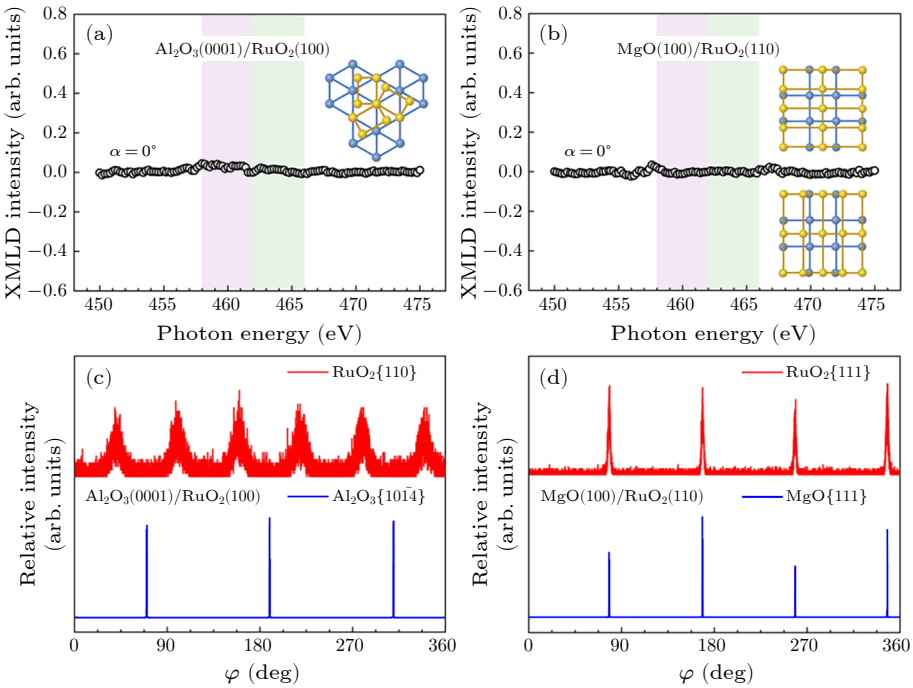

Fig. 4. XMLD and XRD patterns of non-epitaxial RuO_2 films on Al_2O_3 and MgO substrates. (a) XMLD pattern of $Al_2O_3(0001)/RuO_2(100)$ with the inset showing three different matching mode types. (b) XMLD pattern of $MgO(100)/RuO_2(110)$ with the inset showing two different matching mode types. (c) XRD phi-scan of Al_2O_3/RuO_2, where the up (red) and bottom (blue) patterns indicate the $RuO_2(110)$ and $Al_2O_3(10\bar{1}4)$ scanning results. (d) XRD phi-scan of MgO/RuO_2, where the up (red) and bottom (blue) patterns indicate $RuO_2(111)$ and $MgO(111)$ scanning results.

the existence of twin crystals in non-epitaxial RuO_2 films sputtered on $Al_2O_3(0001)$ and $MgO(100)$ substrates, indicating that the counterbalanced in-plane Néel order of different twin crystals accounts for the absence of the characteristic signals of XMLD in such cases.

In summary, we conducted an experimental study on altermagnetic RuO_2 films primarily via X-ray magnetic linear dichroism. The prepared RuO_2 films with different crystalline orientations on various substrates exhibited a desirable crystalline quality and zero net magnetization. The XRD phi-scan patterns revealed the epitaxial growth mode for TiO_2/RuO_2 and MgF_2/RuO_2 and non-epitaxial growth modes for the Al_2O_3/RuO_2 and MgO/RuO_2 samples. Based on the XMLD results, we demonstrated the existence of the Néel order and investigated its spatial relationshipéith the crystalline orientation of RuO_2. (i) The epitaxial $RuO_2(100)$ and $RuO_2(110)$ films exhibited zero-positive-negative-zero XMLD signals below the Néel temperature, clearly demonstrating the existence of the Néel order in RuO_2. (ii) The characteristic XMLD patterns do not appear unless the detection mode of the epitaxial $RuO_2(001)$ films changes from normal incidence to oblique incidence, thus proving that the Néel order is parallel to the [001] crystalline axis in RuO_2. (iii) There are no characteristic XMLD signals corresponding to the Ru M_3-edge for the non-epitaxial RuO_2 films because the in-plane Néel orders of the twin crystals existing in the polycrystalline RuO_2 films cancel each other.

Experimental Methods.

Sample Preparation. RuO_2(15 nm) film samples were prepared on single-crystal $TiO_2(100)$, $TiO_2(110)$, $TiO_2(001)$, $MgF_2(100)$, $MgF_2(110)$, $MgF_2(001)$, $Al_2O_3(0001)$, and $MgO(100)$ substrates via the DC magnetron sputtering method. The RuO_2 layers were deposited by sputtering a Ru target with an $Ar:O_2$ ratio of 4:1 at 773 K. The deposition rate of the RuO_2 films was 3.3 nm/min.

Sample Characterization. Crystal quality and phase composition were analyzed via X-ray diffraction (XRD) characterization utilizing a Rigaku Smartlab instrument with Cu-Kα radiation (wavelength = 0.154 nm). The working voltage and current were set to 40 kV and 150 mA, respectively. The scanning rates were 10°/min and 90°/min for the 2θ-ω scan and phi-scan, respectively. The magnetization of the samples was tested at 300 K using a superconducting quantum interference device (SQUID) from Quantum Design.

XAS and XMLD Measurements. X-ray absorption spectroscopy (XAS) and X-ray magnetic linear dichroism (XMLD) measurements were performed in total-electron-yield mode at the BL08U1A (for conventional tests) and BL07U (for temperature-dependent tests) beamline stations at the Shanghai Synchrotron Radiation Facility. This technique was used to probe the in-plane distribution of the Néel order in the RuO_2 film samples. The detection light spot was $80 \times 80\,\mu m^2$. The incidence angle was 90° (normal incidence) or 45° (oblique incidence). The XMLD curves represent the differences between the normalized linearly vertical (V)- and horizontal (H)-polarized XAS signals.

Acknowledgements. This work was supported by the National Natural Science Foundation of China (Grant

Nos. 12241404, 52225106, and 523B1007) and Open Fund of the State Key Laboratory of Spintronics Devices and Technologies (Grant No. SPL-2401). We acknowledge the BL08U1A and BL07U beamlines at the Shanghai Synchrotron Radiation Facility (SSRF) for the XAS and XMLD measurements.

References

[1] Autieri C 2024 *Nature* **626** 482
[2] Krempaský J, Šmejkal L, D'Souza S W, Hajlaoui M, Springholz G, Uhlířová K, Alarab F, Constantinou P C, Strocov V, Usanov D, Pudelko W R, González-Hernández R, Birk Hellenes A, Jansa Z, Reichlová H, Šobáň Z, Gonzalez Betancourt R D, Wadley P, Sinova J, Kriegner D, Minár J, Dil J H, and Jungwirth T 2024 *Nature* **626** 517
[3] Šmejkal L, Sinova J, and Jungwirth T 2022 *Phys. Rev. X* **12** 031042
[4] Šmejkal L, Sinova J, and Jungwirth T 2022 *Phys. Rev. X* **12** 040501
[5] Šmejkal L, Hellenes A B, González-Hernández R, Sinova J, and Jungwirth T 2022 *Phys. Rev. X* **12** 011028
[6] Yuan L D, Wang Z, Luo J W, Rashba E I, and Zunger A 2020 *Phys. Rev. B* **102** 014422
[7] Hayami S, Yanagi Y, and Kusunose H 2020 *Phys. Rev. B* **102** 144441
[8] Ma H Y, Hu M L, Li N N, Liu J P, Yao W, Jia J F, and Liu J W 2021 *Nat. Commun.* **12** 2846
[9] Liu P F, Li J Y, Han J Z, Wan X G, and Liu Q H 2022 *Phys. Rev. X* **12** 021016
[10] Ahn K H, Hariki A, Lee K W, and Kuneš J 2019 *Phys. Rev. B* **99** 184432
[11] Berlijn T, Snijders P C, Delaire O, Zhou H D, Maier T A, Cao H B, Chi S X, Matsuda M, Wang Y, Koehler M R, Kent P R C, and Weitering H H 2017 *Phys. Rev. Lett.* **118** 077201
[12] Zhu Z H, Strempfer J, Rao R R, Occhialini C A, Pelliciari J, Choi Y, Kawaguchi T, You H, Mitchell J F, Shao-Horn Y, and Comin R 2019 *Phys. Rev. Lett.* **122** 017202
[13] Bai H, Zhang Y C, Han L, Zhou Y J, Pan F, and Song C 2022 *Appl. Phys. Rev.* **9** 041316
[14] Šmejkal L, González-Hernández R, Jungwirth T, and Sinova J 2020 *Sci. Adv.* **6** eaaz8809
[15] González-Hernández R, Šmejkal L, Výborný K, Yahagi Y, Sinova J, Jungwirth T, and Železný J 2021 *Phys. Rev. Lett.* **126** 127701
[16] Šmejkal L, MacDonald A H, Sinova J, Nakatsuji S, and Jungwirth T 2022 *Nat. Rev. Mater.* **7** 482
[17] Machida Y, Nakatsuji S, Onoda S, Tayama T, and Sakakibara T 2010 *Nature* **463** 210
[18] Feng Z X, Zhou X R, Šmejkal L, Wu L, Zhu Z W, Guo H X, González-Hernández R, Wang X N, Yan H, Qin P X, Zhang X, Wu H J, Chen H Y, Meng Z, Liu L, Xia Z C, Sinova J, Jungwirth T, and Liu Z Q 2022 *Nat. Electron.* **5** 735
[19] Tschirner T, Keßler P, Betancourt R D G, Kotte T, Kriegner D, Büchner B, Dufouleur J, Kamp M, Jovic V, Smejkal L, Sinova J, Claessen R, Jungwirth T, Moser S, Reichlova H, and Veyrat L 2023 *APL Mater.* **11** 101103
[20] Cheong S W and Huang F T 2024 *npj Quantum Mater.* **9** 13
[21] Wang M, Tanaka K, Sakai S, Wang Z Q, Deng K, Lyu Y, Li C, Tian D, Shen S C, Ogawa N, Kanazawa N, Yu P, Arita R, and Kagawa F 2023 *Nat. Commun.* **14** 8240
[22] Bose A, Schreiber N J, Jain R, Shao D F, Nair H P, Sun J X, Zhang X S, Muller D A, Tsymbal E Y, Schlom D G, and Ralph D C 2022 *Nat. Electron.* **5** 267
[23] Bai H, Han L, Feng X Y, Zhou Y J, Su R X, Wang Q, Liao L Y, Zhu W X, Chen X Z, Pan F, Fan X L, and Song C 2022 *Phys. Rev. Lett.* **128** 197202
[24] Karube S, Tanaka T, Sugawara D, Kadoguchi N, Kohda M, and Nitta J 2022 *Phys. Rev. Lett.* **129** 137201
[25] Slonczewski J C 1996 *J. Magn. Magn. Mater.* **159** L1
[26] Liu L, Pai C F, Li Y, Tseng H W, Ralph D C, and Buhrman R A 2012 *Science* **336** 555
[27] Bai H, Zhang Y C, Zhou Y J, Chen P, Wan C H, Han L, Zhu W X, Liang S X, Su Y C, Han X F, Pan F, and Song C 2023 *Phys. Rev. Lett.* **130** 216701
[28] Zhang Y C, Bai H, Han L, Chen C, Zhou Y J, Back C H, Pan F, Wang Y Y, and Song C 2024 *Adv. Funct. Mater.* **34** 2313332
[29] Fedchenko O, Minár J, Akashdeep A, D'Souza S W, Vasilyev D, Tkach O, Odenbreit L, Nguyen Q, Kutnyakhov D, Wind N, Wenthaus L, Scholz M, Rossnagel K, Hoesch M, Aeschlimann M, Stadtmüller B, Kläui M, Schönhense G, Jungwirth T, Hellenes A B, Jakob G, Šmejkal L, Sinova J, and Elmers H J 2024 *Sci. Adv.* **10** eadj4883
[30] Lin Z H, Chen D, Lu W L, Liang X, Feng S Y, Yamagami K, Osiecki J, Leandersson M, Thiagarajan B, Liu J W, Felser C, and Ma J Z 2024 arXiv:2402.04995
[31] Hiraishi M, Okabe H, Koda A, Kadono R, Muroi T, Hirai D, and Hiroi Z 2024 *Phys. Rev. Lett.* **132** 166702
[32] Smolyanyuk A, Mazin I I, Garcia-Gassull L, and Valentí R 2024 *Phys. Rev. B* **109** 134424
[33] Stöhr J, Padmore H A, Anders S, Stammler T, and Scheinfein M R 1998 *Surf. Rev. Lett.* **5** 1297
[34] Wu J, Park J S, Kim W, Arenholz E, Liberati M, Scholl A, Wu Y Z, Hwang C, and Qiu Z Q 2010 *Phys. Rev. Lett.* **104** 217204
[35] Wu Y Z, Sinkovic B, Won C, Zhu J, Zhao Y, and Qiu Z Q 2012 *Phys. Rev. B* **85** 134436
[36] Grigorev V, Filianina M, Bodnar S Y, Sobolev S, Bhattacharjee N, Bommanaboyena S, Lytvynenko Y, Skourski Y, Fuchs D, Kläui M, Jourdan M, and Demsar J 2021 *Phys. Rev. Appl.* **16** 014037
[37] Huang Y H, Yang C Y, Cheng C W, Lee A, Tseng C H, Wu H, Pan Q J, Che X Y, Lai C H, Wang K L, Lin H J, and Tseng Y C 2022 *Adv. Funct. Mater.* **32** 2111653
[38] Meng J W, Chen K, Mijit E, Chen D F, Choueikani F, Zou Z Q, Wang L L, Mu G, Geng W P, Kong Q Y, Jiang A Q, Ning X J, and Weng T C 2019 *Phys. Rev. Appl.* **12** 044010
[39] Kuch W, Offi F, Chelaru L I, Wang J, Fukumoto K, Kotsugi M, Kirschner J, and Kuneš J 2007 *Phys. Rev. B* **75** 224406
[40] Schlueter C, Yang N, Mazzoli C, Cantoni C, Tebano A, Di Castro D, Balestrino G, Orgiani P, Galdi A, Herrero-Martín J, Gargiani P, Valvidares M, and Aruta C 2020 *Adv. Quantum Technol.* **3** 2000016
[41] Wu H, Zhang H T, Wang B M, Groß F, Yang C Y, Li G F, Guo C Y, He H R, Wong K, Wu D, Han X F, Lai C H, Gräfe J, Cheng R, and Wang K L 2022 *Nat. Commun.* **13** 1629
[42] Yang M, Li Q, Wang T, Hong B, Klewe C, Li Z, Huang X, Shafer P, Zhang F, Hwang C, Yan W S, Ramesh R, Zhao W S, Wu Y Z, Zhang X X, and Qiu Z Q 2022 *Phys. Rev. B* **106** 214405
[43] Song J H, Chen Y S, Chen X B, Khan T, Han F R, Zhang J N, Huang H L, Zhang H, Shi W X, Qi S J, Hu F X, Shen B G, and Sun J R 2020 *Phys. Rev. Appl.* **14** 024062
[44] Song J H, Chen Y S, Chen X B, Wang H X, Khan T, Han F R, Zhang J N, Huang H L, Zhang J, Zhang H R, Zhang H, Yan X, Qi S J, Hu F X, Shen B G, Yu R C, and Sun J R 2019 *Phys. Rev. Appl.* **12** 054016
[45] Telling N D, Keatley P S, van der Laan G, Hicken R J, Arenholz E, Sakuraba Y, Oogane M, Ando Y, Takanashi K, Sakuma A, and Miyazaki T 2008 *Phys. Rev. B* **78** 184438

[46] Nolting F, Legut D, Rusz J, Oppeneer P M, Woltersdorf G and Back C H 2010 *Phys. Rev. B* **82** 184415
[47] Lee H G, Wang L F, Si L, He X Y, Porter D G, Kim J R, Ko E K, Kim J, Park S M, Kim B, Wee A T S, Bombardi A, Zhong Z C, and Noh T W 2020 *Adv. Mater.* **32** 1905815
[48] Khalid M, Setzer A, Ziese M, Esquinazi P, Spemann D, Poppl A and Goering E 2010 *Phys. Rev. B* **81** 214414
[49] Pereira L M C, Arajo J P, Bael M J V, Temst K and Vantomme A 2011 *J. Phys. D: Appl. Phys.* **44** 215001
[50] Kluczyk P, Gas K, Grzybowski M J, Skupiński P, Borysiewicz M A, Fąs T, Suffczyński J, Domagala J Z, Grasza K, Mycielski A, Baj M, Ahn K H, Výborný K, Sawicki M and Gryglas-Borysiewicz M 2024 *Phys. Rev. B* **110** 155201